Calibration of a Radome-Differential GPS System on a Twin Otter Research Aircraft for Turbulence Measurements

JOHN A. KALOGIROS AND QING WANG

Department of Meteorology, Naval Postgraduate School, Monterey, California

(Manuscript received 11 December 2000, in final form 2 August 2001)

ABSTRACT

A five-hole radome pressure probe at the nose of a small two-engine newly instrumented research aircraft was combined with global positioning system (GPS) receivers in differential mode to obtain high frequency measurements of the wind vector in the atmospheric boundary layer with possible accuracy (root-mean-square error) of about 0.1 m s^{-1}. This low cost and simple system can provide wind velocity measurements of sufficient accuracy to estimate turbulent fluctuations. Special aircraft maneuvers above the atmospheric boundary layer were used to calibrate the radome probe. The analysis of these data showed that the static pressure defect has a significant dependence on flow angles and is affected by the propellers when significant thrust is applied. Using a simple method, the authors found that the pressure distribution on the radome deviated from the one expected for airflow incident on a sphere by more than 5%, the authors also detected a problem in the attack angle differential pressure sensor. The calibration of the local attack and sideslip flow angles due to flow distortion by the aircraft was obtained using two different methods. The first method was a least wind variance one assuming a linear form for the calibration of flow angles. This method is easy to use and can be applied in the presence of turbulence, but does not reveal any possible nonlinear dependence or problems in the data. The second method was a direct one that assumes near–zero mean vertical wind velocity above the boundary layer, while an average horizontal wind was estimated using the airstream speed with respect to the aircraft and the aircraft velocity from the differential GPS data. These methods gave similar results and, thus, increased the reliability of the calibration. The performance of the calibration procedure of the whole system was tested by examining the sensitivity of estimated wind components to the aircraft motion (about 5%) and the quality of mean profiles and turbulence statistics in the boundary layer.

1. Introduction

The Development and Evolution of Coastal Stratocumulus experiment (DECS) took place in June and July 1999 off the coast of Monterey, California, with ultimate goal of understanding the interaction among the coastal mesoscale flow field, the low-level stratocumulus clouds, and the coastal marine boundary layer turbulence. The main volume of measurements of boundary layer turbulence and thermodynamic properties, cloud microphysics, and aerosol physics were made on a two-engine UV-18A Twin Otter (the military version of model Series 300) research aircraft (Fig. 1) operated by the Center for Interdisciplinary Remote Piloted Aircraft Study (CIRPAS) of the Naval Postgraduate School. The Twin Otter is newly equipped with a variety of sensors described in section 2. For the measurement of wind velocity relative to the aircraft, a five-hole radome probe with 33° half-angles was used to minimize the effect of nonspherical shape of the radome (Brown et al. 1983). The position, velocity, and attitude angles (true heading, pitch, and roll) of the aircraft were measured using the global positioning system (GPS) technique. The vector sum of the aircraft velocity and wind relative to the aircraft gives the wind components in the meteorological frame of reference. The well-known wind equations for this estimation given by Lenschow (1986) were used with the inclusion of moist air thermodynamics described by Khelif et al. (1999).

The radome probe for measurement of the air stream vector was introduced by Brown et al. (1983) and it is now used in many research aircraft (Tjernström and Friehe 1991; Khelif et al. 1999). This system has been proved to be capable of providing wind turbulence measurements at scales larger than the diameter of the aircraft's fuselage by measuring the pressure distribution on the nose of the aircraft that changes with incident flow angles (attack and sideslip angles) and airspeed (corresponding to dynamic pressure). This method is simpler, less expensive and avoids the vibration and frequency response problems of a long boom mounted on the nose of the aircraft. However, due to the flow distortion by the aircraft (mainly the upwash induced by the wing vortex) the local flow angles differ from

Corresponding author address: Dr. J. Kalogiros, Dept. of Meteorology, Naval Postgraduate School, S89 Dyer Rd., Monterey, CA 93943.
E-mail: ikalogir@nps.navy.mil

Unauthenticated | Downloaded 12/06/23 05:42 AM UTC

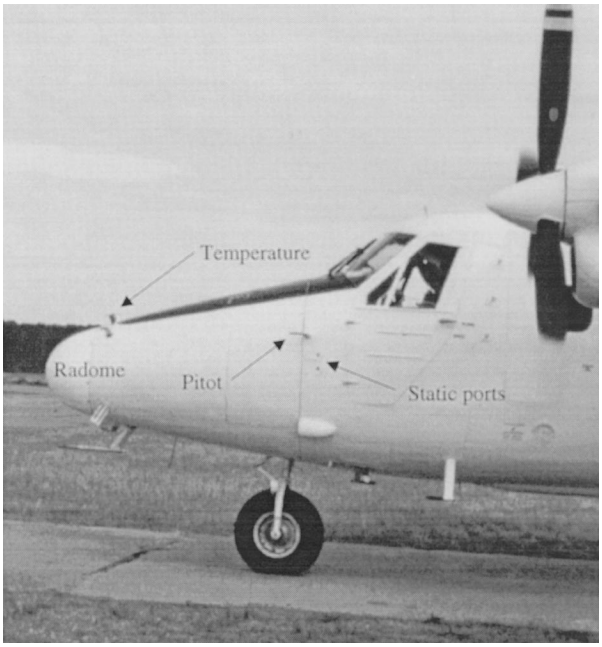

FIG. 1. Photograph of the CIRPAS Twin Otter showing the various probes near the aircraft nose.

those in the free air stream. Therefore, a very careful in-field calibration, which is different for each aircraft, is required (Lenschow 1986; Crawford et al. 1996). The calibration is achieved by analyzing data from special maneuvers that change the speed and attitude angles of the aircraft and are usually performed in the assumed nonturbulent and near homogeneous air above the atmospheric boundary layer.

The development of the Differential GPS (DGPS) method in the last decade promises accuracies in the measurement of the position, velocity, and attitude angles of the aircraft that fulfill the requirements for turbulent wind measurements using research aircraft (Lenschow 1986). Commercial GPS systems allow now for a high sampling rate and they are relatively inexpensive, drift-free and quite smaller and lighter compared to inertial navigation systems (INS).

In this paper, the method to calibrate the radome system using special aircraft maneuvers in the nonturbulent air above the boundary layer is described. The calibration includes the correction of the static pressure defect, the correction of the radome differential pressures for the nonspherical shape of the radome, and the calibration of attack and sideslip angles for the flow distortion by the aircraft. The performance of the calibration procedure and the quality of measurements of the radome/DGPS system are verified by examining the contamination of the estimated wind components by the aircraft motion during the maneuvers and the quality of sample mean profiles and turbulence statistics (spectra) in the boundary layer.

2. Instrumentation

The main instrumentation of the CIRPAS Twin Otter aircraft is given in Table 1. The TANS Vector system uses a four-antenna array in a cross configuration and measures the attitude angles (true heading, pitch, and roll) of the array from differential phase measurements of the GPS signal. The center point of measurement of the attitude angles is the cross point of the TANS Vector axes located on the longitudinal axis of the aircraft about 5.5 m from the radome. Additional sensors for the measurement of air temperature, humidity, and air stream vector (a Rosemount 858 five-hole probe under the right wing) were also installed on the aircraft for redundancy purposes. Other instrumentation included shortwave and longwave radiation sensors, a sea surface temperature sensor, a Gerber Particulate Volume Monitor for measurement of liquid water, a Forward Scattering Spectrometer Probe for measurements of droplet spectra, a

TABLE 1. Main instrumentation on the CIRPAS/NPS Twin Otter research aircraft.

Parameter	Sensor	Location	Accuracy	Sampling rate
Position/velocity	Novatel 3951 GPS	Cabin/ground station	5 m/0.05 m s^{-1}	10 Hz/2 Hz
Attitude angles (including heading)	Trimble Navigation TANS Vector	Fuselage	0.05°−0.1°	10 Hz
Acceleration	3-axes accelerometers	Cabin		100 Hz
Static pressure	Setra 270	Fuselage (pilot static port)	0.53 hPa	100 Hz
Dynamic pressure	Rosemount 1221F	Fuselage (copilot Pitot)	0.20 hPa	100 Hz
Total pressure	Setra 270	Radome (center port)	0.25 hPa	100 Hz
Differential pressure for attack angle	Rosemount 1221F	Radome (attack angle ports at ±33° angles)	0.20 hPa	100 Hz
Differential pressure for sideslip angle	Validyne	Radome (sideslip angle ports at ±33° angles)	0.20 hPa	100 Hz
Temperature	Non-deiced Rosemount 102E4AL housing, platinum wire	Radome	0.5°C	100 Hz
Humidity	Slow dewpoint hygrometer	Fuselage	0.5°C	10 Hz
	Lyman-α, InfraRed Gas Analyzer (IRGA)	Fuselage		100 Hz
	Aerodyne Inc.	Fuselage		10 Hz

Unauthenticated | Downloaded 12/06/23 05:42 AM UTC

Passive Cavity Aerosol Spectrometer Probe, and a new Cloud, Aerosol, and Precipitation Spectrometer.

The sampling frequency of the sensors used in the calculation of turbulent fields was 100 Hz. Data were stored using 16-bit analog-to-digital converters for high resolution in the expected range of measurements. The high sampling rate for turbulent measurements is required because of the high speed of the aircraft relative to the wind speed, even though in our case it was just 50–80 m s^{-1} (a typical speed value of other research aircraft is about 100 m s^{-1}). The ground station GPS receiver was sampled at 2 Hz, which is an adequate sampling rate since its position was fixed. This receiver was used in differential mode with the GPS receiver on the aircraft, which was sampled at 10 Hz covering the possible frequency range of aircraft motions. Using data when the aircraft was steady on the ground before takeoff (static tests), accuracies (root-mean-square error) of 2 m in the horizontal and 5 m in vertical position, and 0.02 m s^{-1} in the horizontal and 0.05 m s^{-1} in the vertical velocity of the aircraft were found similar to the results of Dobosy et al. (1996). The accuracy of TANS Vector system improves with increasing antenna separation (4 m in our case), but long arrays require more time for integer lock (integrity check of the integer part of the phase differences) and are not as rigid as short ones. We estimated a 0.05°–0.1° accuracy from the random noise of our ground data before takeoff, which is about the accuracy given by the manufacturer.

The high accuracy measurement of the aircraft motion is expected to improve significantly the accuracy of the inferred wind velocity components. The error analysis of the wind equations by Tjernström and Friehe (1991) for a radome system combined with an INS system showed that the typical error for the horizontal wind components is 0.1 and 0.2 m s^{-1} for the vertical wind component without including the INS error for the aircraft velocities. They used an error of 0.2° for the aircraft attitude angles and somewhat large errors for the differential pressure sensors (0.4 hPa). Using the results of the relative error analysis of the wind equations by Tjernström and Friehe and our instruments' accuracies given in Table 1, we conclude that the expected (lowest possible) typical total error (including the error in aircraft velocities) in our case is 0.1 m s^{-1} for the horizontal wind components and 0.15 m s^{-1} for the vertical wind component. This expected accuracy is based on the measurement uncertainty of the instruments and the actual accuracy of the system depends on the calibration procedure described below.

3. System calibration

The data used in the calibration process came from in-flight maneuvers above the boundary layer and takeoff periods during three experimental days (17, 19, and 22 July 1999) resampled at 1 Hz. This low sampling rate is adequate for the analysis of slow maneuvers in low turbulence air. Data were first forward and reverse (for zero phase distortion) low-pass filtered with an eighth order Butterworth digital filter at Nyquist frequency (0.5 Hz) to avoid aliasing. The maneuvers performed by the aircraft were speed runs, sideslip (or yaw) maneuvers, pitch maneuvers, and reverse heading maneuvers (Lenschow 1986). The pitch maneuvers were not used in the final calibration because of relatively large changes of altitude (more than 100 m) and large vertical velocities of the aircraft which resulted in changes of attack angle that were smaller than the corresponding changes during speed runs. All maneuvers were used for testing the quality of the calibration. We estimate the average gross weight of the aircraft to be about 4900 kg and the flaps were up during the maneuvers.

The altitude measurement provided by the DGPS system often showed sharp changes of several meters induced by the techniques (such as cycle slip detection and least-squares adjustment) used in the software for the differential correction of GPS data. A corrected altitude was obtained combining the low frequency content of the DGPS altitude measurement with the high frequency content of the altitude estimated by integration of the measurement of the vertical velocity of the aircraft with the DGPS. The latter measurement is directly based on the Doppler shift of the GPS carrier signal and, thus, software errors are smaller in this case compared to the case of position estimates.

An installation misalignment error of the main axis of the TANS Vector system relative to the longitudinal axis of the aircraft by about 10° was found comparing the indicated aircraft heading with the track angle during takeoff runs. The track angle is the angle of the horizontal velocity of the aircraft with respect to the north and it was estimated by the horizontal components of the aircraft velocity with respect to the earth given by the Novatel DGPS system. Heading and track angles should be equal when the aircraft is moving on the runway. The heading alignment error also induced an error in the pitch angle of the aircraft, which was clearly observed during the reverse heading maneuvers. The correction of this error required calculation of the aircraft attitude angles in the aircraft coordinate system rotated relative to the TANS Vector axes. The takeoff runs were also used for the detection of possible calibration offsets different from laboratory calibrations in the static pressure, total pressure, and dynamic pressure measurements using the known atmospheric wind conditions during those time periods from a nearby surface meteorological station.

Measured air temperature was corrected for the compressibility effect using a recovery factor that minimized the variation of temperature with Mach number during the speed runs. This method will also correct for the effect of airflow distortion by the aircraft at the probe location (Cooper and Rogers 1991). The correction factor $\eta = (T_t - T_r)/T_r$, where T_t and T_r are the total and

Unauthenticated | Downloaded 12/06/23 05:42 AM UTC

recovery temperatures respectively, was assumed to be a linear function of Mach number M within the small range of M values (0.15–0.25) that the Twin Otter flies. The values of η against M were found to be of the same order of magnitude (10^{-4}) as the ones given by Rosemount for the 102E4AL housing model (Rosemount 1981).

The local attack α and sideslip β flow angles (spherical coordinates) at the radome were calculated using the exact nonlinear equations (Crawford and Dobosy 1992) for angle pressure ports located at $\alpha_p = \beta_p = 33°$ from the center port of the near spherical radome:

$$\alpha = -\frac{1}{2}\sin^{-1}\left(\frac{4}{9}\frac{\Delta P_\alpha}{P_d \cos\beta \sin 2\alpha_p}\right) \quad (1a)$$

$$\beta = -\frac{1}{2}\sin^{-1}\left(\frac{4}{9}\frac{\Delta P_\beta}{P_d \cos^2\alpha \sin 2\beta_p}\right) \quad (1b)$$

$$P_{tr} - P_s = \frac{P_d}{4}(9\cos^2\alpha\cos^2\beta - 5). \quad (1c)$$

These equations are valid for incompressible flow and they make an approximation of the pressure field for the low Mach number values (less than 0.3) that the Twin Otter flies. The pressure differences ΔP_α (top–bottom) and ΔP_β (right–left when facing the aircraft) are measured by the attack and sideslip pressure ports, P_{tr} is the pressure measured at the center port (the design stagnation point) of the radome, P_s is the static pressure measured on the fuselage (see section 1a) and P_d is the free airstream dynamic pressure. This nonlinear system of three equations has three unknowns (α, β, and P_d) and was solved with an iterative method designed for fast convergence. The cross-dependence of α and β included in the above equations is significant for large flow angles that occur during strong updrafts/downdrafts and lateral winds or during the aircraft maneuvers. Before solving the system of Eqs. (1a)–(1c) the measured P_{tr} has to be corrected for the compressibility effect (Lenschow 1986) using the compressible Bernoulli equation for isentropic processes (Shevell 1989). This correction is needed because dynamic pressure is defined as $(1/2)\rho U^2$, where ρ and U are the variable air density (compressible flow) and speed, respectively, and it is not the same as the difference between total pressure and static pressure. The correction corresponds to a maximum of 0.7 hPa decrease for our relatively slow aircraft with maximum dynamic pressure of the airstream up to 40 hPa.

a. Static pressure defect

The static pressure on commercial aircraft is measured from ports at proper locations on the fuselage that depend on the aircraft design. In our case, the static pressure ports were located on both sides of the fuselage, just in front of the cockpit (Fig. 1). The dynamic pressure P_d was estimated as the difference between the total pressure by a Pitot tube at the copilot side and the static pressure using a differential pressure transducer. This dynamic pressure was corrected for the compressibility effect similarly with the radome ''total'' pressure P_{tr} mentioned above. Well-designed Pitot probes show very small sensitivity to flow angles up to 20° and, thus, a zero position error of measured total pressure is usually assumed. The measured static pressure, however, deviates from that in the free airstream due to the flow distortion by the aircraft. This error is the position error or static pressure defect dP_s (defined as measured local static pressure P_{sm} minus free airstream static pressure P_s) and is usually estimated using a trailing cone system (Brown 1988; Khelif et al. 1999), so that the static pressure of the undisturbed air behind the aircraft is measured. Because such a system was not available, a different approach (Tjernström and Friehe 1991; Bögel and Baumann 1991) was used, which is based on the hydrostatic balance assumption in the free atmosphere above the boundary layer. We note that the trailing cone system limits the maneuvers that can be performed by some aircraft and is required to be at the same altitude with the aircraft, so that no altitude error is introduced in the estimation of static pressure defect. The dynamic pressure P_d is computed from the difference between total pressure and static pressure and, thus, contains a $-dP_s$ error.

We used data from the speed runs and sideslip maneuvers to find the dependence of static pressure defect on dynamic pressure P_d, attack angle α, and sideslip angle β. Usually the angle dependence of static pressure defect, which is more significant at low airstream speed (relatively large flow angles) as in our case, is not considered. Bögel and Baumann (1991) found a significant angle dependence of static pressure defect for a 858AJ Rosemount probe mounted on a boom at the nose of a Falcon aircraft. In our approach, the static pressure during the maneuvers was corrected for altitude changes relative to the altitude of the first data point of each maneuver using the hydrostatic balance assumption. We used the corrected DGPS altitude measurement as described in the beginning of section 3. Then, the static pressure defect was computed as the difference of this height adjusted static pressure with its value at that first point of each maneuver. This procedure actually computes the static pressure defect minus its value at the first point of each maneuver leg. Thus, the constant term of the fit of the computed static pressure defect by a polynomial function of the flow parameters P_d, α, and β [see Eq. (2) below] cannot be determined in this way.

A first approximation of this term was found by requiring in-flight maneuvers data to match the static pressure defect estimates obtained during takeoff runs using as a reference the average value of static pressure before the aircraft starts to increase speed. This takeoff static pressure defect includes the effect of the proximity to the ground and the takeoff configuration of the flaps

Unauthenticated | Downloaded 12/06/23 05:42 AM UTC

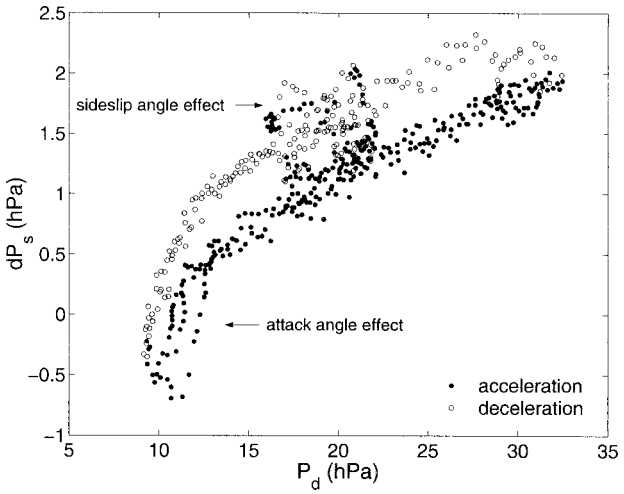

FIG. 2. The static pressure defect dP_s as a function of Pitot dynamic pressure P_d for the speed run and sideslip maneuver on 17 Jul 1999.

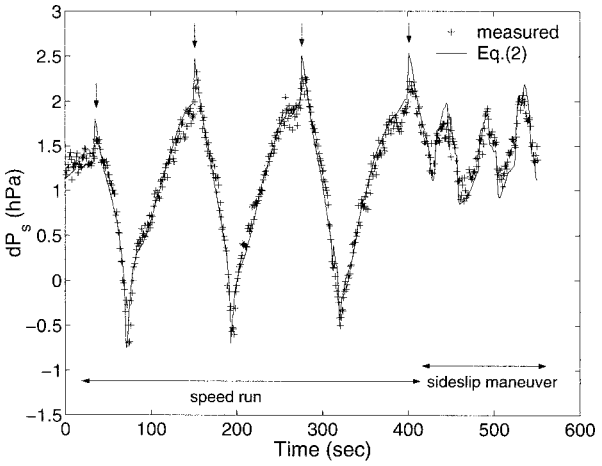

FIG. 3. Time series of static pressure defect measured and approximated by Eq. (2) for the same data shown in Fig. 2.

and, thus, it is different from the in-flight data. Using data just after takeoff, when the aircraft was at an altitude of two to three times the wing span and the hydrostatic balance assumption for height adjustment, we found that the proximity to the ground may increase the static pressure defect by about 0.4 hPa relative to the in-flight conditions. However, these data were of limited length with significant scatter. An accurate estimate of the constant term in the static pressure defect approximation was obtained from the reverse heading maneuvers by minimizing the differences between the wind components before and after the turn (see section 3d). The longitudinal wind component in the aircraft frame of reference is more sensitive to the correct removal of the static pressure defect, since it is directly connected to the airstream speed and, thus, dynamic pressure. This step was performed at the end of the calibration process described in the next paragraphs and the process was repeated using the new accurate constant term of the static pressure defect approximation.

Figure 2 shows the computed static pressure defect dP_s for the case of 17 July 1999 maneuvers as a function of dynamic pressure P_d. As it can be seen in Fig. 2, the dP_s corresponding to longitudinal acceleration (with respect to earth) of the aircraft is lower by about 0.5 hPa with respect to deceleration. This implies that the flow around the aircraft is different in these two cases, which has also been observed by Tjernström and Friehe (1991). As it is shown by Kalogiros and Wang (2002, manuscript submitted to *J. Atmos. Oceanic Technol.*) this was mainly the effect of the aircraft propellers' slipstream (tube of high speed) at the position of the static pressure sensor (see Fig. 1). Figure 2 also shows the static pressure defect, which deviates significantly from a second-order polynomial of P_d for large attack and sideslip angles at the points indicated by the arrows. The dependence of dP_s on P_d, α, and β was approximated in a least absolute error sense (robust estimation of the parameters of the fit to avoid data outliers) by the following equation:

$$\begin{aligned} dP_s &= P_{sm} - P_s \\ &= C_0 + 0.964 \times 10^{-1} P_d - 0.522 \times 10^{-3} P_d^2 \\ &\quad - 1.131 P_d \alpha^2 + 0.531 P_d \beta^2, \end{aligned} \tag{2}$$

where

$$C_0 = \begin{cases} -0.489 & \text{for aircraft acceleration} \\ 0.041 & \text{for aircraft deceleration,} \end{cases}$$

on average during the maneuvers. The units of the angles and the pressures are radians and hectoPascals, respectively. The local flow angles at the radome used in the fit were computed using the Pitot measured P_d in Eqs. (1a) and (1b), because of the less noisy differential measurement of P_d compared to the postcalculation of P_d using P_{tr} and P_s in Eq. (1c).

During the speed run maneuvers, the positive acceleration values were in the range 0 to 1 m s^{-2} (0.53 m s^{-2} median value) and the negative ones were in the range -0.5 to -1.5 m s^{-2} (-0.81 m s^{-2} median value). During normal flight conditions (almost no acceleration from changes in engines' thrust) a linear interpolation of C_0 to zero acceleration ($C_0 = -0.278$), assuming that the values of C_0 reported just after Eq. (2) correspond to the above median acceleration values, was used. In Eq. (2) we note the quadratic (symmetric) dependence of dP_s on flow angles, which was evident from the time series of dP_s (especially during the sideslip maneuvers with large positive and negative angle values of sideslip angle).

Figure 3 shows the time series of dP_s measured against the one approximated by Eq. (2) for the speed run and sideslip maneuvers on 17 July 1999. The sudden increases of dP_s at its local maxima indicated by arrows during the speed run correspond to abrupt changes from

Unauthenticated | Downloaded 12/06/23 05:42 AM UTC

acceleration to deceleration of the aircraft. Most of the time the error of the approximation is within ± 0.2 hPa, which is quite low if one considers the validity of hydrostatic balance assumption and the accuracy of the DGPS altitude measurements.

b. *Correction for the nonspherical shape of the radome*

We performed a simple check to detect any possible deviation of the pressure distribution on the radome from the spherical model Eqs. (1a)–(1c). The pitot measured dynamic pressure P_d used in these equations was corrected for the static pressure defect as well as static pressure P_s. In the case of very small sideslip angle (speed run) or attack angle (sideslip maneuver) Eq. (1c) can be solved for the remaining flow angle. Then, the corresponding pressure difference ΔP_α or ΔP_β can be estimated from Eqs. (1a)–(1b). Equation (1c) is expected to hold for the near spherical radome because the true stagnation point is very close (flow angles up to 15°) to the design stagnation point (the center port) where ''total'' pressure P_{tr} is measured. The differential pressure ports are located at 33° from the center port and, thus, their measurements may depart significantly from Eqs. (1a)–(1b). Figures 4a and 4b show the estimated pressure differences for the attack and sideslip pressure ports against the measured ones for the speed run and the sideslip maneuver, respectively, on 22 July 1999. The deviation of the experimental data from the theoretical model is significant (more than 5%) and, thus, the pressure differences should be corrected before being used for the estimation of local flow angles with Eqs. (1a)–(1c). We note that the deviation is of opposite sign between attack angle and sideslip angle ports, implying a different shape of the radome on those two axes. However, errors in the laboratory calibration of the differential sensors may contribute to this behavior, too. Using the above test we found large scatter for the maneuver data on 19 July 1999 and thus, they were not used in the radome calibration below.

The measured ΔP_α in Fig. 4a has been actually corrected for a small near linear dependence on the acceleration of the aircraft with unknown origin (probably a problem of the corresponding sensor). This was concluded from the correlation of the original measured ΔP_α with the estimated one (similar to Fig. 4a), which showed a looplike behavior (even though with considerable scatter). Most of this looplike behavior and scatter could be removed if a dependence of measured ΔP_α on the aircraft acceleration during the speed run maneuver is assumed. If ΔP_α is not corrected for this dependence, the result is a looplike behavior in the calibration plot of the radome local attack angle against the estimated free airstream one (see Fig. 5a). This would suggest an unrealistic large dependence of the attack angle calibration and, thus, of the upwash/flow distortion effect on the acceleration of the aircraft. We note that a small

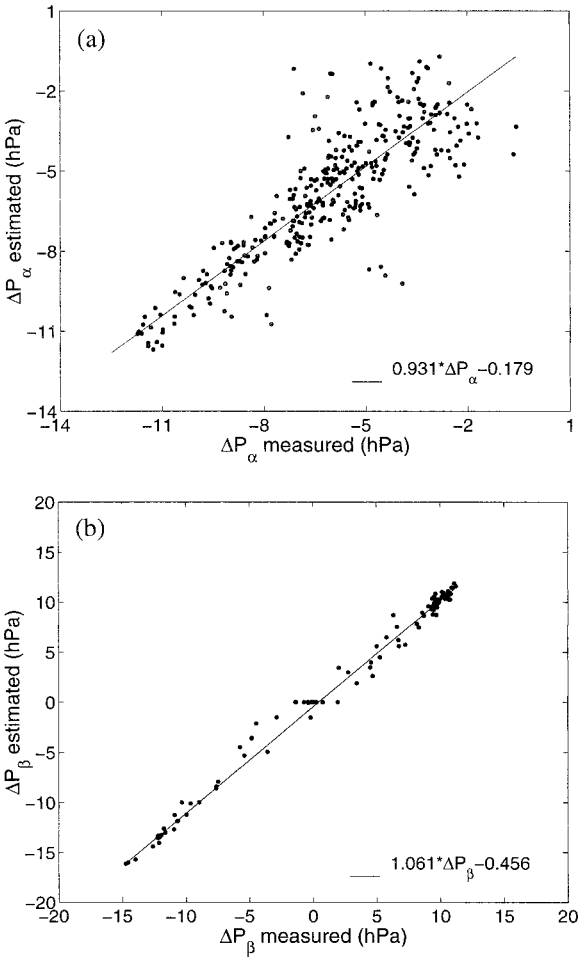

FIG. 4. Estimated pressure differences for (a) the attack and (b) sideslip pressure ports against measured ones for the speed run and the sideslip maneuver, respectively, on 22 Jul 1999. The solid lines correspond to the best linear fits given in the figures.

dependence is actually expected mainly because of the suction effect of the propeller's slipstream at the nose of the aircraft as it is shown by Kalogiros and Wang (2002, manuscript submitted to *J. Atmos. Oceanic Technol.*).

c. *Variance method of radome calibration*

A commonly used technique to calibrate the local flow angles at the radome so that they correspond to true free airstream flow angles is to calculate the calibration factors that minimize the variance of the wind components (Tjernström and Friehe 1991; Khelif et al. 1999). The assumption made here is that errors in the estimation of the free air stream flow angles increase the wind variance. This method is easy to use and can be applied in the presence of turbulence in the boundary layer, but does not reveal any possible nonlinear dependences or problems in the data.

In the application of this method we assumed a linear

Unauthenticated | Downloaded 12/06/23 05:42 AM UTC

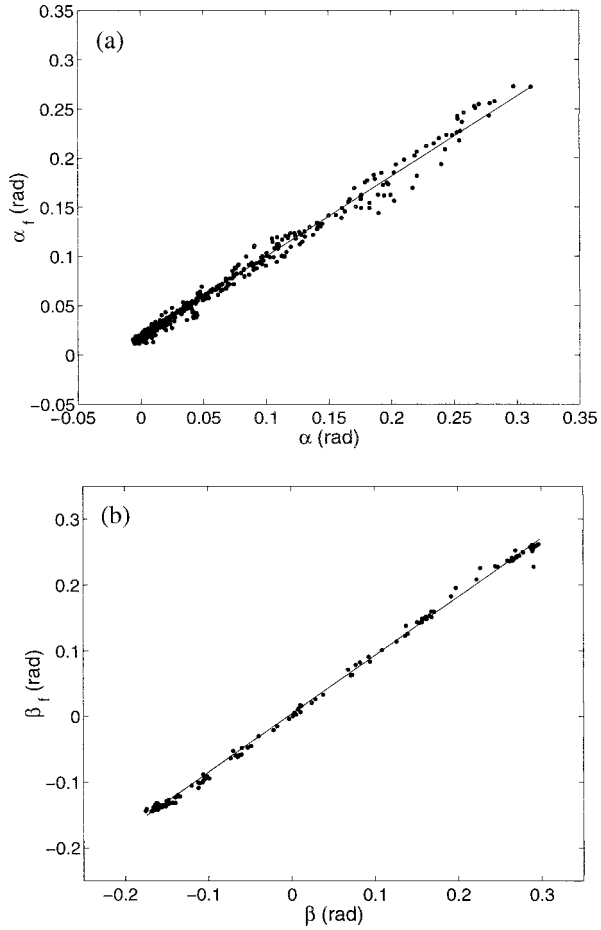

FIG. 5. The estimated free airstream flow angles (a) α_f and (b) β_f against the corresponding radome local flow angles α and β for the speed run and sideslip maneuvers, respectively, performed on 22 Jul 1999. The solid lines are best fit ones given by Eqs. (6a) and (6b).

dependence of free airstream flow angles to local flow angles α and β with no cross-dependence. The full equations for the estimation of wind components in the meteorological frame of reference were used. The calibration coefficients (slope and offset) were assumed to be independent of the Mach number, which is justified by the small range (0.15–0.25) of Mach number at which the Twin Otter flies. For faster aircraft that fly in a broader range of Mach number, these coefficients are found to be slowly varying functions of the Mach number (Brown et al. 1983; Tjernström and Friehe 1991). We computed the calibration coefficients that minimized the sum of the horizontal wind components variances and the second moment of vertical wind velocity. We used the second moment of vertical wind velocity instead of the variance so that the mean vertical wind velocity was also minimized. The calibration coefficients were computed using all the maneuver data for each experimental day. The following calibration equations were obtained (angles in rad):

$$\alpha_f = 0.811\alpha + 0.0193 \quad (3a)$$

$$\beta_f = 0.889\beta - 0.0106, \quad (3b)$$

where α_f and β_f are the free airstream attack and sideslip flow angles, respectively. Using the data from 17 July and 22 July 1999 we found substantially different calibration coefficients (especially for the attack angle). The values of the coefficients in Eqs. (3a) and (3b) correspond to the latter day. The decision of using the results of this day was based on the analysis described in the next section.

d. Direct method of radome calibration

In order to detect possible problems in the maneuver data, we used an additional direct approach for the calibration of the radome probe. In this approach we estimated the average wind vector for each speed run or sideslip maneuver. We assumed zero average vertical wind velocity, as it is usually done in such calibrations above the boundary layer. The average horizontal wind was estimated by a fit of the following equation to the experimental data:

$$U_a^2 = U_p^2 + U_w^2 - 2U_pU_w \cos(t_p - d_w). \quad (4)$$

This equation comes out from the fact that the vector sum of the aircraft velocity and the wind relative to the aircraft (airstream) gives the horizontal wind components in the meteorological frame of reference assuming a zero mean vertical wind velocity. The measured quantities are the free airstream speed relative to the aircraft U_a (true airspeed), and the inertial speed and track angle of the aircraft relative to the meteorological frame of reference U_p and t_p, respectively, calculated by the DGPS aircraft velocity data. The unknown constant parameters are the average wind speed and direction in the meteorological frame of reference, U_w and d_w respectively, to be estimated by minimizing an error function (we used the absolute error) of U_a estimated by Eq. (4) against measured U_a.

Next, we transformed the estimated wind components to airstream components in the aircraft reference system using the inverse transform of the one described by Lenschow (1986) for the calculation of the wind components in the meteorological frame of reference. The airstream velocity components in the aircraft system u_a, v_a, and w_a are related to airstream flow angles through the following equations (Crawford and Dobosy 1992):

$$u_a = -U_a \cos\alpha_f \cos\beta_f \quad (5a)$$

$$v_a = -U_a \cos\alpha \sin\beta_f \quad (5b)$$

$$w_a = -U_a \sin\alpha_f. \quad (5c)$$

The flow angles α_f and β_f are spherical coordinates similar to Eqs. (1a)–(1c). The corresponding wind components defined by Lenschow (1986) are somewhat different because in that case α_f is not a spherical coor-

Unauthenticated | Downloaded 12/06/23 05:42 AM UTC

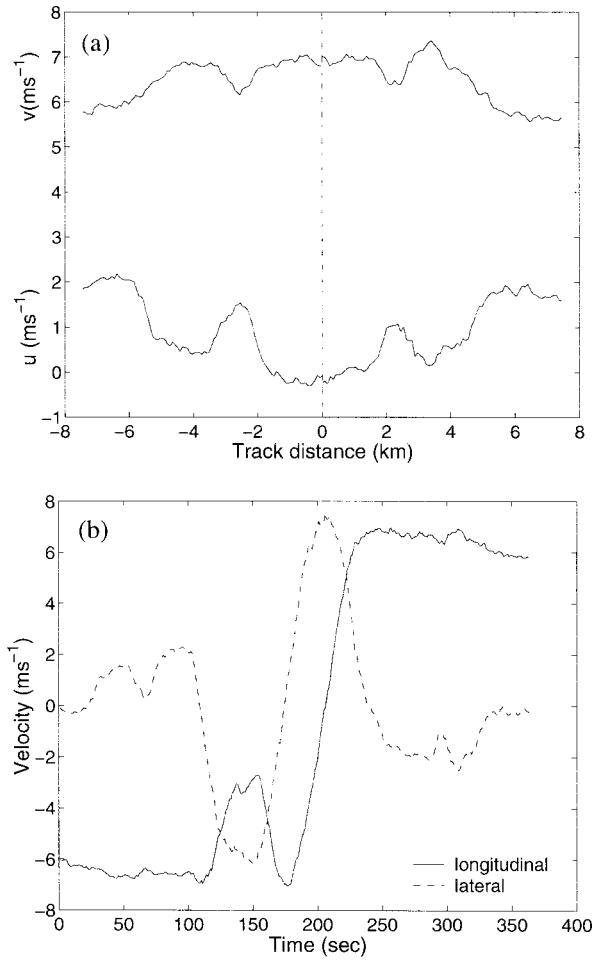

FIG. 6. Horizontal wind components estimated using a −0.0087 sideslip calibration offset for the two near parallel paths with opposite heading of the reverse heading maneuver on 22 Jul 1999 (a) in the meteorological reference system (u, v: east and north velocity components, respectively), and (b) in the aircraft reference system.

dinate. According to Eqs. (5a)–(5c), the free airstream flow angles can be estimated as $\beta_f = \tan^{-1}(v_a/u_a)$ and $\alpha_f = \tan^{-1}(\cos\beta_f w_a/u_a)$.

Figures 5a and 5b show the estimated free airstream flow angles α_f and β_f, respectively, against the corresponding local flow angles α and β at the radome for the maneuvers performed on 22 July 1999. Cases with absolute sideslip angle greater than 0.05 rad (about 3°) were not included in the calibration of attack angle in Fig. 5a. The attack angle results for the data from 17 July 1999 showed a nonlinear dependence at small angles resulting in an erroneous calibration offset and, thus, they were rejected from the radome calibration. The following calibration equations were obtained:

$$\alpha_f = 0.814\alpha + 0.0186 \quad (6a)$$

$$\beta_f = 0.889\beta + C_\beta. \quad (6b)$$

The value of the calibration offset of the sideslip angle C_β was estimated to be 0.0062 using the method described above. Most of the dispersion around the solid lines especially for attack angle values above 0.15 rad (8.5°) is probably due to wind variations during the maneuvers. Alternatively, we can use the time derivative of the wind equations (Lenschow 1986) assuming zero vertical wind velocity, steady (in the small time period and space of each maneuver) wind components and small roll, pitch, and attack angles to find an estimate of the time derivative of the β_f angle during the sideslip maneuvers. The correlation between the time derivatives of β and β_f gave a similar result with Eq. (6b) for the slope coefficient but in our case the dispersion of the data points was larger than the one in Fig. 5b, probably because the time derivative amplified the noise in the data.

The calibration coefficients in Eqs. (6a)–(6b) are very close to the ones in Eqs. (3a)–(3b), which were estimated using the variance method, with the exception of the offset of the sideslip angle. A careful analysis revealed that an error of 0.5 m s^{-1} in the horizontal wind components estimated using Eq. (4) could even change the sign of C_β. However, the slope coefficient was less sensitive to such errors. Thus, we used the reverse heading maneuver data with the slope coefficient given by Eq. (6b) to estimate C_β. The wind component that is more sensitive to the value of the calibration offset of the sideslip is the lateral one in the aircraft frame of reference, since it is directly connected to the sideslip angle. The value of the calibration offset of the sideslip angle found by minimizing the differences between the average estimated wind components in the meteorological frame of reference for the legs before and after the turn of the reverse heading maneuver was $C_\beta = -0.0087$. This value is very close to the value of the calibration offset of the sideslip angle given by Eq. (3b). In the data analysis presented in the next paragraphs the radome calibration given by Eqs. (6a) and (6b) with the above value of C_β was used.

The results of the procedure for the estimation of the above sideslip offset are shown in Fig. 6, where the wind varies along the maneuver legs but with similar horizontal variations between the forward and backward legs. Track distance is the distance from a common point of the two legs along the aircraft track, where negative distance means that the aircraft approaches that point. We note that the assumption that the wind components in the aircraft system should have the same magnitude but change sign (this can be seen in Fig. 6b) is often used in the reverse heading maneuver. However, this requires an exact reverse maneuver, which is not usually the case. We used the more general method of minimizing the change of the components of the wind in the meteorological frame of reference during the maneuver.

4. Calibration performance

a. Maneuvers results

The reverse heading maneuver is a good test for the quality of the estimation of the horizontal components

Unauthenticated | Downloaded 12/06/23 05:42 AM UTC

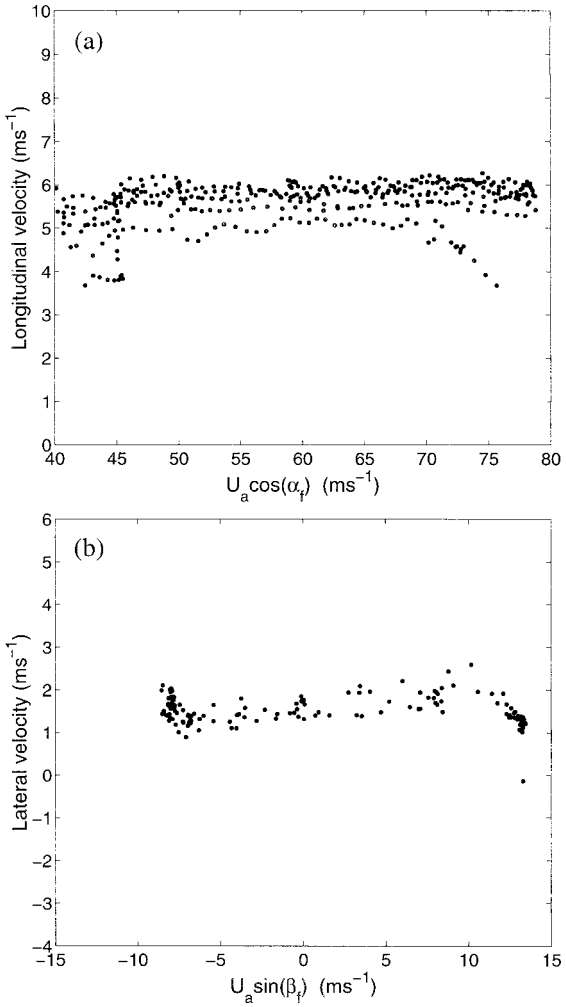

FIG. 7. Estimated (a) longitudinal and (b) lateral component of the horizontal wind with respect to the average heading direction of the aircraft against the corresponding airspeed components for the speed run and the sideslip maneuver, respectively, on 22 Jul 1999.

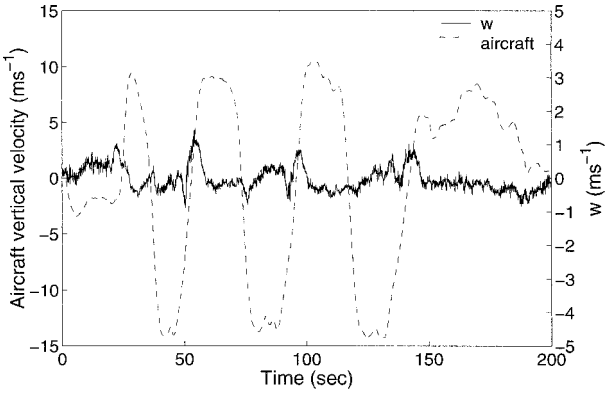

FIG. 8. Time series (20 Hz) of the estimated vertical wind velocity w and the vertical velocity of the aircraft w_p for the pitch maneuver on 22 Jul 1999.

of the wind, which depend mainly on the accuracy of airstream speed U_a and sideslip angle. The corresponding average horizontal wind components for each of the two legs of the reverse maneuver shown in Fig. 6a agree with each other within 0.1 m s^{-1}. Figures 7a and 7b show the estimated wind longitudinal and lateral components of the horizontal wind with respect to the average heading direction of the aircraft against the corresponding airspeed components $U_a \cos\alpha_f$ and $U_a \sin\beta_f$ for the speed run and the sideslip maneuver, respectively, on 22 July 1999. The results satisfy adequately (about 5% root-mean-square error) the commonly used criterion of 10% contamination error for the quality of the performance of the system (Lenschow 1986).

Figure 8 shows time series of the estimated vertical wind velocity w and the vertical aircraft velocity w_p for the pitch maneuver on 22 July 1999. We use 20-Hz data to show the response of the system during possible fast variations of the vertical velocity of the aircraft. The pitch maneuvers are the most demanding ones for testing the contamination of the vertical component of the wind by the motion of the aircraft because of the large vertical velocity of the aircraft involved. Our results in Fig. 8 show very small correlation of the estimated vertical wind velocity with the vertical velocity of the aircraft for most of the time during the pitch maneuver. The deviation of the estimated vertical wind velocity from near zero values occurs at time periods of fast changes of the vertical velocity of the aircraft, when the airflow around the aircraft is highly unsteady. Figures 9a and 9b are scatter diagrams of w against w_p and the corresponding airspeed component $U_a \sin\alpha_f$. From these figures it can be concluded that the root-mean-square error of the vertical wind velocity, which is assumed to have near zero mean value in the air where the maneuvers took place, is about 5% of the vertical velocity of the aircraft and is not significantly correlated with it or the corresponding air stream component. However, we can see from Fig. 8 that the instantaneous error of the vertical wind velocity during abrupt changes of the vertical velocity of the aircraft can increase significantly.

b. Boundary layer results

In this section sample results from the DECS boundary layer data at about 0930 local time on 7 July 1999 (a day with limited stratocumulus cloud cover over the experimental area) are presented as a quality test of profile and turbulent wind statistics. The raw 100-Hz data were filtered at 10-Hz Nyquist frequency to avoid aliasing and resampled at 20 Hz. The 10-Hz DGPS data showed very little spectral energy above 2 Hz (not shown here) and, thus, it was plausible to linearly interpolate them to 20 Hz. Static pressure was low-pass filtered at 3 Hz to suppress the observed high frequency noise. A simple analysis of the equations (Lenschow 1986) used to derive the wind components shows that dynamic pressure variations dominate over the static

Unauthenticated | Downloaded 12/06/23 05:42 AM UTC

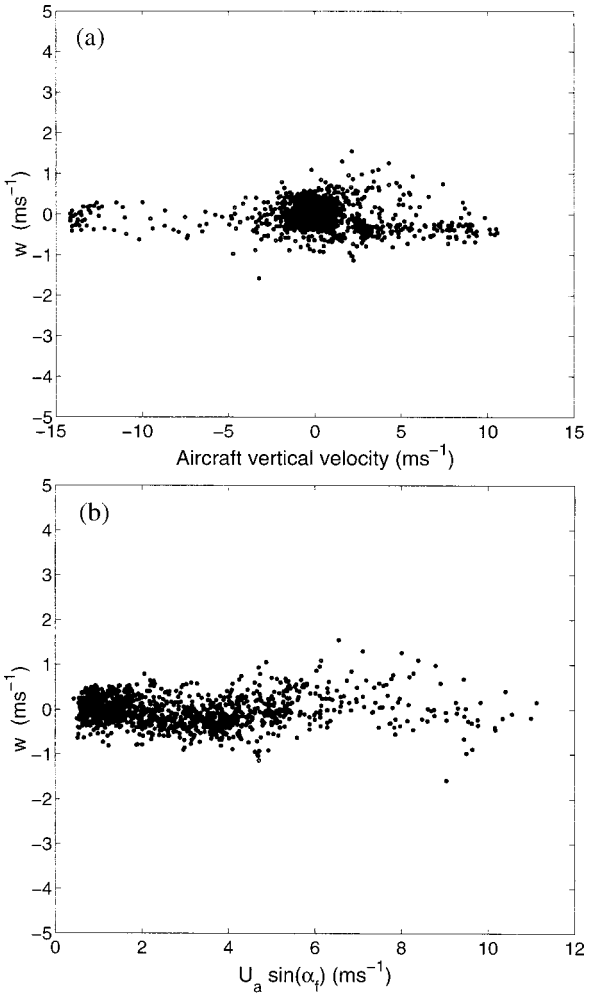

FIG. 9. Scatter diagrams of the estimated vertical wind velocity w against (a) vertical velocity of the aircraft w_p and (b) airspeed component $U_a \sin\alpha_f$ for all the maneuver data on 22 Jul 1999.

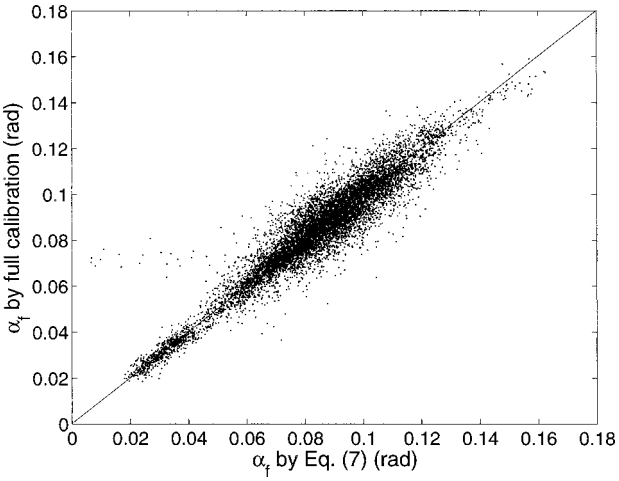

FIG. 10. Free airstream attack angle α_f estimated by Eq. (7) with $w = 0$ against the one estimated using the radome calibration given by Eq. (6a) and the removal of the slow variation in the offset of ΔP_α described in section 4b for the entire flight on 7 Jul 1999. The solid line is the equality line.

pressure variations at high frequencies. Thus, this filtering does not affect significantly the high-frequency content of the wind estimates.

Applying the calibration procedure described in section 3 to normal flight data we found that the average vertical wind velocity during some flights was different than the expected near zero value in the boundary layer. The cause was a slow variation of the offset of the correction of ΔP_α for the nonspherical radome (section 3b) during the flight and we had to filter it out. This is probably a slow change of the calibration offset of the corresponding differential pressure sensor or the result of changes in the weight of the aircraft (fuel burn). A final check of the attack angle calibration was possible using the entire data of each flight and the approximate equation for the calculation of vertical wind velocity (Lenschow 1986):

$$w = -U_a \sin(\theta - \alpha_f) + w_p, \qquad (7)$$

where θ is the pitch angle of the airplane. Then, the α_f values estimated by Eq. (7) with w set to zero should on the average fall around the equality line when plotted against the α_f values obtained using the full calibration procedure described in section 3 [Eqs. (6)] and the removal of the slow variation in the offset of ΔP_α. A comparison plot is shown in Fig. 10 for the 1-Hz measurements on 7 July 1999. The random dispersion of the data points on this plot is the result of turbulence.

Figures 11a–d show profiles (20-point moving averages) of wind speed and direction, potential temperature, and water vapor specific humidity from a vertical spiral sounding (ascent followed by descent). A nearly well-mixed layer up to 230 m and a strong temperature inversion in the layer 450–650 m can be seen in these figures. The diameter of the spiral was 7 km and the aircraft horizontal velocity was higher by 10 to 20 m s^{-1} during descent compared to ascent. Despite the change of airplane heading during the spiral motion and the difference in horizontal velocity of the aircraft between ascent and descent, the corresponding wind speed and direction profiles display the same layer structures especially above 450 m. Between 250 and 450 m, a difference in the boundary layer structure among ascent and descent is evident in the virtual temperature and water vapor mixing ratio profiles in addition to the wind profile.

Figure 12 shows the power spectra of the wind velocity components with respect to the sampling direction and the virtual temperature from a 30-km straight level leg at an altitude of about 36 m above the sea surface. The sampling direction (convection velocity) of a moving platform (aircraft) is the air stream direction. The airstream vector is the vector difference of wind speed and aircraft velocity. The average wind direction in the case of Fig. 12 is 335°, the aircraft path (track) direction

Unauthenticated | Downloaded 12/06/23 05:42 AM UTC

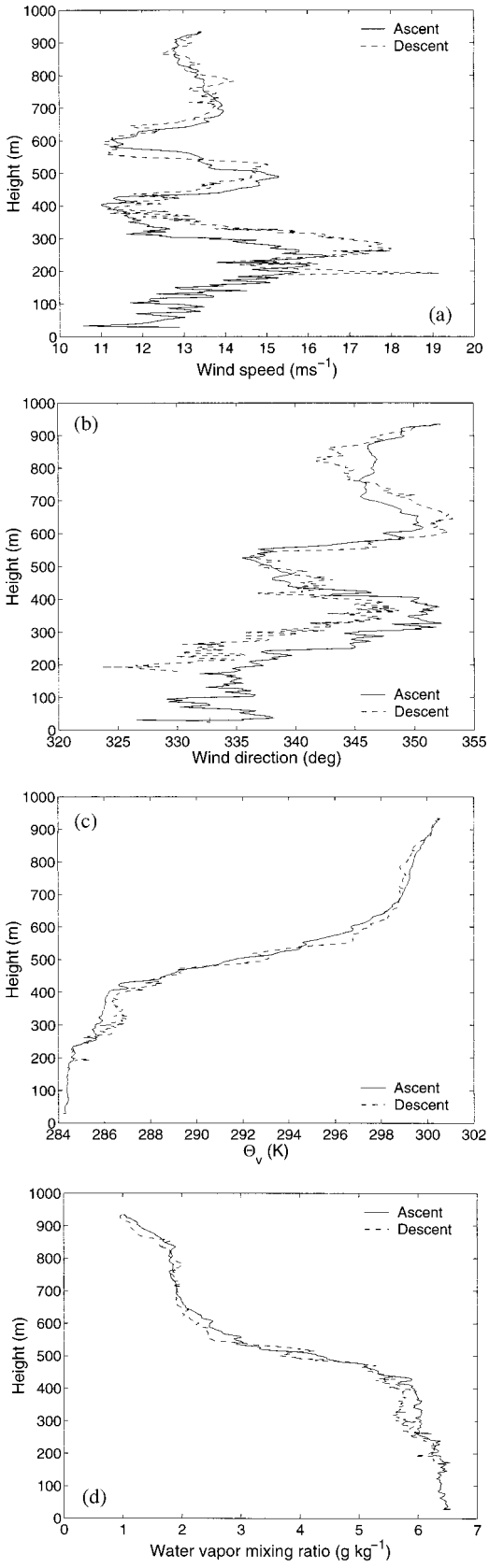

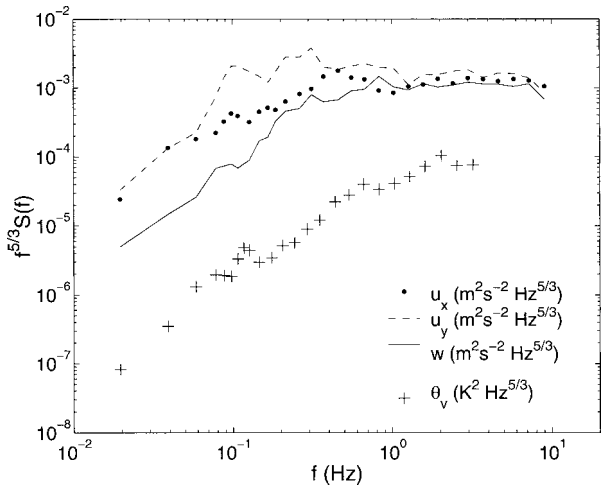

FIG. 12. Power spectra $S(f)$ where f is frequency, of u_x (wind velocity component along the average airstream vector), u_y (lateral component of the wind velocity), w (vertical wind velocity), and θ_v (virtual potential temperature) from a 30-km straight level leg at about 36 m above the sea surface on 7 Jul 1999. The power spectra have been divided by the inertial subrange behavior $f^{-5/3}$.

is 87°, and sampling direction is 75°, almost perpendicular to the average wind direction. The spectra are averaged over segments of 1024 points and then smoothed over equal logarithmic intervals of frequency. The virtual potential temperature time series were quite noisy above 3 Hz and, thus, the corresponding spectra are shown only up to this frequency. All the power spectra show a well-defined isotropic inertial subrange with the expected $-5/3$ slope above 2 Hz and no evident contamination aircraft motions at low frequencies. At frequencies higher than 8 Hz, the drop of the power spectra is due to the antialiasing filter. The power spectrum of the longitudinal component falls off less rapidly because it is affected by high frequency (mainly above 10 Hz) noise of the raw data. The power spectrum of the lateral wind component (which is almost along the mean wind direction) shows significant low frequency–mesoscale energy in the frequency decade just before the inertial subrange as opposed to the vertical wind component. These spectral properties are consistent with the idea of elongation of eddies of the along wind component due to stretching by the mean wind shear (Nicholls and Readings 1981). Thus, when sampling is in the across wind direction, energy from small wavenumbers in the spectrum of the along wind component is redistributed to larger wavenumbers (higher frequencies).

Figure 13 shows the cospectra of momentum and heat fluxes for the same measurement leg with Fig. 12. The cospectra seem to approach the expected inertial sub-

←

FIG. 11. Profiles of (a) wind speed, (b) direction, (c) virtual potential temperature, and (d) water vapor mixing ratio from a vertical spiral sounding on 7 Jul 1999.

Unauthenticated | Downloaded 12/06/23 05:42 AM UTC

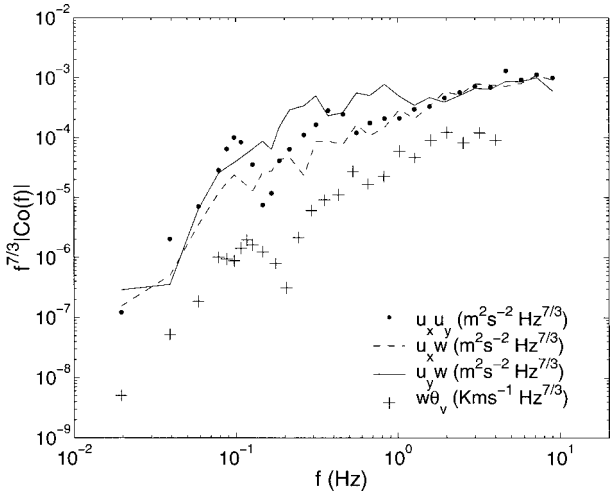

FIG. 13. Absolute cospectra $|\mathrm{Co}(f)|$ of the wind components and θ_v (virtual potential temperature) for the same time period with Fig. 12. The cospectra have been divided by the inertial subrange behavior $f^{-7/3}$.

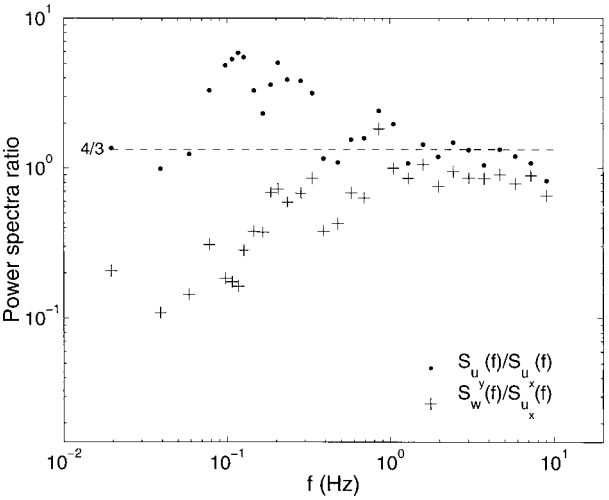

FIG. 14. Ratios of the power spectra of u_y and w to the power spectrum of u_x for the same time period with Fig. 12. The dash line is the 4/3 ratio expected by local isotropy in the inertial subrange.

range slope of $-7/3$ above 2–3 Hz (we note, however, that there is not sufficient bandwidth above these frequencies) and, thus, they adequately cover the significant energy-containing region even at this low altitude. The isotropic behavior in the inertial subrange requires just that the turbulent fluxes are zero or decreasing faster than the power spectra in this range (Kaimal and Finnigan 1994) as shown in Fig. 13.

Figure 14 shows power spectra ratios of vertical and lateral wind components to the power spectrum of the longitudinal wind component with respect to the sampling direction for the same flight leg with Fig. 12. In the sampling direction, frequency corresponds to the wavenumber component on this direction according to Taylor's hypothesis of frozen turbulence. Thus, the above ratios of the frequency power spectra of the velocity components in the inertial subrange should be 4/3 according to local isotropy (Kaimal and Finnigan 1994), which is a very good test of the quality of the radome calibration. Figure 14 shows that for the lateral wind velocity the ratio is very close to the isotropic value in the inertial subrange, while for the vertical wind velocity it is lower than unity. This behavior was repeated in almost all of the experimental days. Similar behavior of the vertical wind velocity spectrum is found in the results of other researchers using aircraft measurements over sea (Nicholls and Readings 1981; Tjernström and Friehe 1991) or over land (Lenschow et al. 1991). The drop of the power spectra ratios above 8 Hz is due to the antialiasing filter and the high frequency noise of the longitudinal component discussed above. Kalogiros and Wang (2002, manuscript submitted to *J. Atmos. Oceanic Technol.*) show that the observed lower than unity S_w/S_{u_x} ratio in the inertial subrange is not an indication of deviation from local isotropy, but an effect related to aerodynamic response of the wing vortex and, thus, of the induced upwash at the nose of the aircraft. They propose, also, a method to correct the time series of the vertical wind velocity or its power and cross spectra with other parameters using in-flight fast acceleration measurements.

5. Conclusions

Based on to the results of this work, a radome system can be combined with a DGPS system to provide in-situ turbulence wind measurements of high quality (expected root-mean-square error of about 0.1 m s^{-1}) and frequency in the boundary layer with small cost. The altitude measurements by the DGPS system seem to have software related occasional problems that can be corrected using the relatively accurate measurements of vertical velocity of the aircraft. The heading angle measurement with GPS (TANS Vector system) is possible to have a misalignment error with the aircraft main axis, which is easily detected and corrected using data on the runway before takeoff.

A careful calibration of the system using a process like the one described in section 3 should include the dependence of static pressure defect on the flow angles and a verification of the approximation of nearly spherical radome. The assumption of hydrostatic balance above the boundary layer was successfully used in the modeling of static pressure defect without a trailing cone. The analysis of static pressure defect data showed that the flow around the aircraft is affected by the aircraft propellers' slipstream and, thus, it has different characteristics in acceleration periods compared to deceleration periods of the aircraft during the maneuvers. The process of correction for possible significant departure from the spherical shape of the radome can also reveal possible problems in the differential pressure sensors.

Unauthenticated | Downloaded 12/06/23 05:42 AM UTC

The method involves an independent estimate of the flow angles at the radome during the maneuvers using the pressure at the center port of the radome. A direct method for the radome calibration based on the assumption of constant wind components during the maneuvers was described in section 3d. The use of additional methods, like the minimum variance method, for the radome calibration increased the reliability of the calibration.

The maneuver results showed a quite small (about 5%) contamination error (root mean square) by the velocity components of the aircraft. The normal flight results indicated that the system accurately resolves the isotropic behavior of the power spectra of the estimated wind components in the inertial subrange.

Acknowledgments. The present work was sponsored by the National Science Foundation (NSF) Grant ATM9900496. The authors would like to thank Haf Jonsson at CIRPAS for his endless efforts in improving the measurements capability of the CIRPAS Twin Otter and particularly for his efforts in setting up the turbulence measurement capability. We are grateful to Djamal Khelif for providing information on the arrangement of the instruments on the aircraft and the photograph of the CIRPAS Twin Otter shown in Fig. 1. We would also like to thank Richard Friesen, Donald Lenschow, and Ian MacPherson for their valuable comments on the manuscript.

REFERENCES

Bögel, W., and R. Baumann, 1991: Test and calibration of the DLR Falcon wind measuring system by maneuvers. *J. Atmos. Oceanic Technol.,* **8,** 5–18.

Brown, E. N., 1988: Position error calibration of a pressure survey aircraft using a trailing cone. NCAR Tech. Rep. NCAR/TN-313+STR, 29 pp.

——, C. A. Friehe, and D. H. Lenschow, 1983: The use of pressure fluctuations on the nose of an aircraft for measuring air motion. *J. Climate Appl. Meteor.,* **22,** 171–180.

Cooper, W. A., and D. Rogers, 1991: Effects of airflow trajectories around aircraft on measurements of scalar fluxes. *J. Atmos. Oceanic Technol.,* **8,** 66–77.

Crawford, T. L., and R. J. Dobosy, 1992: A sensitive fast-response probe to measure turbulence and heat flux from any airplane. *Bound.-Layer Meteor.,* **59,** 257–278.

——, ——, and E. J. Dumas, 1996: Aircraft wind measurement considering lift-induced upwash. *Bound.-Layer Meteor.,* **80,** 79–94.

Dobosy, R. J., T. L. Crawford, R. T. McMillen, and E. J. Dumas, 1996: Accurate aircraft wind measurements using the global positioning system (GPS). *Proc. Second Int. Airborne Remote Sensing Conf. and Exhibition,* Vol. I, San Francisco, CA, ERIM International, 221–227.

Kaimal, J. C., and J. J. Finnigan, 1994: *Atmospheric Boundary Layer Flows: Their Structure and Measurement.* Oxford University Press, 289 pp.

Kalogiros, J. A., and Q. Wang, 2002: Aerodynamic effects on wind turbulence measurements with research aircraft. *J. Atmos. Oceanic Technol.,* submitted.

Khelif, D., S. P. Burns, and C. A. Friehe, 1999: Improved wind measurements on research aircraft. *J. Atmos. Oceanic Technol.,* **16,** 860–875.

Lenschow, D. H., 1986: Aircraft measurements in the boundary layer. *Probing the Atmospheric Boundary Layer,* D. H. Lenschow, Ed., Amer. Meteor. Soc., 39–55.

——, E. R. Miller, and R. B. Friesen, 1991: A three-aircraft intercomparison of two types of air motion measurements systems. *J. Atmos. Oceanic Technol.,* **8,** 41–50.

Nicholls, S., and C. J. Readings, 1981: Spectral characteristics of the surface layer turbulence over the sea. *Quart. J. Roy. Meteor. Soc.,* **107,** 591–614.

Rosemount, 1981: Total temperature sensors. Rosemount Engineering Company Tech. Bull. 5755, Rev. A, 28 pp. [Available from Rosemount Eng. Co., P.O. Box 35129, Minneapolis, MN 55435.]

Shevell, R. S., 1989: *Fundamentals of Flight.* Prentice Hall, 438 pp.

Tjernström, M., and C. A. Friehe, 1991: Analysis of a radome air-motion system on a twin-jet aircraft for boundary-layer research. *J. Atmos. Oceanic Technol.,* **8,** 19–40.

Unauthenticated | Downloaded 12/06/23 05:42 AM UTC